

## High-pressure structural transition and magnetic phase diagram of $\text{CuB}_2\text{O}_4$

Subodha Sahoo,<sup>1,2</sup> Pallavi Malavi<sup>1</sup>, and S. Karmakar<sup>1,2,\*</sup>

<sup>1</sup>*HP & SRPD, Bhabha Atomic Research Centre, Trombay, Mumbai 400085, India*

<sup>2</sup>*Department of Physical Sciences, Homi Bhabha National Institute, Anushaktinagar, Mumbai 400094, India*

 (Received 26 December 2022; revised 17 February 2023; accepted 2 March 2023; published 13 March 2023)

Noncentrosymmetric  $\text{CuB}_2\text{O}_4$  is a prototypical system with interacting spin sublattices of different dimensionality, exhibiting diverse magnetic structures and magnetic phase transitions. Here we report pressure-induced structural evolution of  $\text{CuB}_2\text{O}_4$  and its effect on the magnetic phase diagram. Powder x-ray diffraction (XRD), Raman scattering, and infrared phonon measurements have been performed under high pressure at room temperature. Although XRD shows lattice stability up to  $\sim 25$  GPa, Raman and IR phonon measurements reveal structural anomaly near 3 GPa, followed by a structural phase transition at  $\sim 12$  GPa. Pressure evolution of the zero-phonon lines in the low-temperature optical absorption studies helps identifying the symmetry change of the Cu sites modifying the crystal-field energy levels at the structural transition. High-pressure magnetization measurements have been performed with magnetic field applied perpendicular to the tetragonal  $c$  axis. With increasing pressure the saturation magnetization of the commensurate weak ferromagnetic phase increases with systematic reduction of its turnover critical field. Pressure-induced systematic suppression of the dc susceptibility in this phase is attributed to the reduced critical field, indicating pressure-driven enhanced stability of the weak ferromagnetic phase at high pressure. Whereas, below 10 K the critical field of the incommensurate-commensurate transition increases with pressure, indicating enhanced stability of the incommensurate helical order at high pressure.

DOI: [10.1103/PhysRevB.107.094411](https://doi.org/10.1103/PhysRevB.107.094411)

### I. INTRODUCTION

Copper metaborate ( $\text{CuB}_2\text{O}_4$ ) crystallizes in the tetragonal noncentrosymmetric space group  $I42d$ . This is an intriguing magnetic insulator exhibiting diverse and intricate magnetic structures and magnetic transitions due to essentially the presence of two distinct spin subsystems of different dimensionality and strength [1–3]. While  $\text{Cu}^{2+}$  ( $3d^9$ ) ions at the crystallographic  $4b$  sites (Cu1) form a three-dimensional Heisenberg antiferromagnetic strong spin subsystem  $A$ , those at  $8d$  sites (Cu2) form a quasi-one-dimensional zigzag spin-chain subsystem  $B$  (see Fig. 1). For both the subsystems, apart from spin interactions via superexchange paths (Cu-O-B-O-Cu) and easy-plane anisotropic exchange, relativistic Dzyaloshinskii-Moriya (DM) interactions come into play due to the broken inversion symmetry [4–9]. The magnetic phase diagram of  $\text{CuB}_2\text{O}_4$  has been extensively studied at zero field as well as under magnetic field applied in different crystallographic axes revealing a large set of magnetic structures, as has been elaborated in a recent report [10]. Various measurement techniques, viz., magnetization, specific heat, electron spin resonance, muon spin rotation, NMR, neutron diffraction, inelastic neutron scattering, magnetostriction, and thermal conductivity measurements have been employed over more than two decades to understand the spin structures and intra- and intersublattice spin interactions [1–3,5–7,10–16]. At zero field, a canted antiferromagnetic commensurate (C) spin order in the tetragonal  $ab$  plane is established

in the strong  $A$  spin subsystem below the Néel temperature  $T_N = 20$  K, whereas the interchain frustration (shown by the dashed line in Fig. 1) keeps the weak  $B$  spin subsystem in the paramagnetic state. Below  $T^*$  ( $\sim 10$  K) both subsystems enter into an incommensurate (IC) helical spin structure with  $T$ -dependent propagation vector along the crystallographic  $c$  axis [3], although partial spin fluctuation persists in the  $B$  subsystem down to 0.3 K [13]. A weak ferromagnetic order emerges in the commensurate phase upon application of a small magnetic field [10], whereas application of magnetic field drives the IC phase into the C phase via an intermediate incommensurate phase  $\text{IC}'$  with a different propagation vector [7,15,16]. Although the chiral magnetic ordering and the incommensurate-commensurate transition have been theoretically explained by the presence of the antisymmetric DM interaction that acts as the Lifshitz invariant term and also supported by the spontaneous formation of the soliton lattice [4,7,17], a complete understanding is far from over, especially due to the emergence of many unknown IC phases at further low temperatures [11,13,14].

In the commensurate weakly ferromagnetic (WFM) phase of  $\text{CuB}_2\text{O}_4$ , simultaneous breaking of time-reversal symmetry and lattice inversion symmetry gives rise to remarkable nonlinear optical properties and also intriguing magnetoelectric properties. The observed magnetic field induced second harmonic generation (SHG) has been a powerful tool to establish the magnetic phase diagram and has helped unambiguous identification of the site-selective crystal-field split  $d-d$  transitions [18]. The electric (magnetic) field control of magnetization (electric polarization) has been reported in Ni-doped  $\text{CuB}_2\text{O}_4$  crystal [19,20]. Nonreciprocal directional

\*sdak@barc.gov.in

dichroism [21,22], antiferromagnetic linear dichroism [23], direction-dependent luminescence [24], nonreciprocal refraction of light [25], and toroidal nonreciprocity of optical SHG [26] are some of the novel optical magnetoelectric properties that have been discovered in  $\text{CuB}_2\text{O}_4$ . Because of the extreme sensitivity to the spin structure, the linear dichroism measurement has been able to identify the elliptical spiral spin structures and its subtle transitions within the incommensurate phase [23,27], apart from resolving the dispute over an experimental claim of the magnetic control of crystal chirality [28,29].  $\text{CuB}_2\text{O}_4$  is the first antiferromagnetic (AFM) insulator where visible light absorption helps unambiguous identification of the complete set of zero-phonon  $d-d$  transitions of the Jahn-Teller  $\text{Cu}^{+2}$  ions, providing genuine crystal-field parameters [30]. Frenkel exciton and its Davydov split multiplets have been uniquely identified in  $\text{CuB}_2\text{O}_4$  by high-resolution magnetoabsorption studies [31]. Novel optical magnetoelectric properties have been attributed to the strong spin-orbit coupling (SOC) driven orbital hybridization that modifies the electric- and magnetic- dipole transition probabilities [22,24,32]. An unconventional nature of the  $d-d$  excitations has also been revealed in  $\text{CuB}_2\text{O}_4$  by the Cu  $K$  edge resonant inelastic x-ray scattering (RIXS) measurements [33]. The complete set of zone-center phonons and two-magnon excitation in the antiferromagnetic  $\text{CuB}_2\text{O}_4$  were investigated in detail by polarization-dependent Raman and IR spectroscopic studies [34,35]. A recent study has reported somewhat weaker spin-phonon coupling in this compound as compared to other cuprates [36]. The tetragonal structure of  $\text{CuB}_2\text{O}_4$  is found stable over the wide  $T$  range [3]. As pressure tuning of the structural parameters is a powerful tool to study the interplay between various magnetic interactions, high-pressure investigation of  $\text{CuB}_2\text{O}_4$  is of immense interest to explore for possible new magnetic phases and evolution of magnetic phase diagram. To the best of our knowledge, no high-pressure studies have so far been reported on  $\text{CuB}_2\text{O}_4$ . Here, we report pressure-induced structural evolution and its effect on magnetic phases in  $\text{CuB}_2\text{O}_4$  by powder x-ray diffraction, Raman scattering, and infrared phonon, optical absorption, and magnetization measurements. While the tetragonal structure is found stable up to  $\sim 25$  GPa, Raman and IR phonon measurements reveal anomalous change of pressure dependence of phonon frequency near 3 GPa, followed by a structural phase transition at  $\sim 12$  GPa. Optical absorption measurement at low temperature gives clear evidence of Cu( $8d$ ) site symmetry change above 10 GPa associated with the structural transition. High-pressure magnetization measurements have been performed on single crystals with magnetic field applied perpendicular to the tetragonal  $c$  axis. While hydrostatic pressure favors commensurate WFM order above  $T^*$ , pressure stabilizes incommensurate helical spin structure below  $T^*$ .

## II. EXPERIMENTAL METHODS

$\text{CuB}_2\text{O}_4$  single crystals were grown by high-temperature solution growth method by mixing high-purity CuO and  $\text{B}_2\text{O}_3$  in 1:20 molar ratio, where  $\text{B}_2\text{O}_3$  was used as flux. The mixture was first homogenized for 48 h at  $980^\circ\text{C}$  and then cooled at  $750^\circ\text{C}$  at a cooling rate of  $1^\circ\text{C}/\text{h}$ . The crystals

were grown in a platinum crucible. Single crystals of few millimeter size are synthesized at the bottom of the crucible. The crystal was finely ground to characterize by powder x-ray diffraction measurement and the lattice parameters are found in good agreement with the reported values [37]. Due to the three-dimensional (3D) atomic arrangement, the crystals are difficult to cleave in a particular orientation. For diamond-anvil cell (DAC) based high-pressure studies on single crystals, crystal flakes of  $\sim 20$  micrometers thick are obtained by breaking the as-grown crystal and their wide surface orientation is identified by Laue's back reflection method. We have succeeded in selecting tiny single crystals with flat (010) and (001) surfaces.

High-pressure powder x-ray diffraction (XRD) measurements on  $\text{CuB}_2\text{O}_4$  at room temperature have been performed at the XRD1 (wavelength  $0.7 \text{ \AA}$ ) and XPRESS (wavelength  $0.4957 \text{ \AA}$ ) beamlines of the Elettra Synchrotron, Trieste, Italy. A finely ground sample was loaded in a Stuttgart type DAC (culet diameter  $500 \mu\text{m}$ , hardened steel gasket preindented to  $50 \mu\text{m}$  thickness and hole diameter  $120 \mu\text{m}$ ). Methanol-ethanol-water (MEW) (16:3:1) and silicone oil were used as pressure transmitting medium (PTM) in two sets of measurements. The two-dimensional diffraction images were recorded on image plate detectors and these were converted to  $I-2\theta$  diffraction profiles using the FIT2D software [38]. Structural analyses were performed using the EXPGUI software [39]. High-pressure IR reflectance measurements at room temperature have been performed at the SISSI beamline of Elettra Synchrotron using an IR microscope equipped with a liquid helium cooled bolometer detector and coupled to a Bruker IFS66v interferometer, which allowed DAC based measurements in the frequency range  $150-900 \text{ cm}^{-1}$ . Synthetic type-IIa low fluorescence diamond anvils (of culet size  $500 \mu\text{m}$ ) were used for Raman and IR measurements. A plate type (001) oriented single crystal (thickness  $\sim 20 \mu\text{m}$  and lateral dimension  $\sim 150 \mu\text{m}$ ) is placed in the preindented gasket hole (hardened steel,  $50 \mu\text{m}$  thick,  $180 \mu\text{m}$  hole diameter), which is then filled with KCl powder as pressure medium. For high-pressure Raman measurements, oriented single crystal is mounted in a DAC (as used in IR measurements) with MEW as pressure medium. Raman spectra were recorded in a backscattering geometry using a Horiba LABRAM HR Spectrometer with DPSS lasers of wavelengths 532 and 633 nm (focus spot size  $\sim 10 \mu\text{m}$ , laser power 1 mW, acquisition time 300 s). The spectra were collected by a liquid nitrogen cooled CCD spectrometer.

For optical absorption studies under high pressure and at low temperature, a clamp type DAC (culet diameter  $400 \mu\text{m}$ , hardened steel gasket, preindented to  $60 \mu\text{m}$  thickness and hole diameter  $120 \mu\text{m}$ ) has been loaded with an oriented crystal flake ( $\sim 20 \mu\text{m}$  thick) with NaCl as pressure medium and was mounted in a liquid helium flow cryostat KONTI (Cryovac). The monochromatic light (in the range  $1.2-3.5 \text{ eV}$ ) from a grating monochromator is focused onto the sample using a Schwarzschild objective (spot size  $\sim 20 \mu\text{m}$ ). The transmitted light is measured in the sample-in/sample-out mode by a thermoelectric cooled photomultiplier tube detector using a lock-in technique. In XRD, Raman, IR, and optical absorption measurements, pressures in DAC are measured using the standard ruby luminescence method. High-pressure

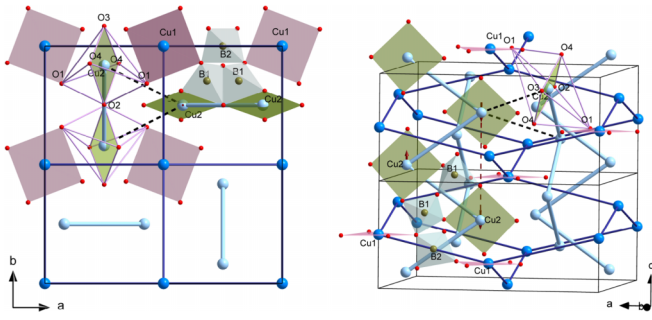


FIG. 1. Crystal structure of  $\text{CuB}_2\text{O}_4$  (space group  $I\bar{4}2d$ ,  $z = 12$ ), as viewed along two different directions. Cu atoms are at two different Wyckoff sites: Cu1 at the  $4b$  site and Cu2 at the  $8d$  site. Cu1 atoms (dark blue) form a three-dimensional (3D) network, whereas Cu2 atoms (light blue) form quasi-one-dimensional (quasi-1D) zigzag chain along the  $c$  axis. Two  $(\text{Cu1})\text{O}_4$  squares (pink) are connected through a  $(\text{B2})\text{O}_4$  tetrahedron, whereas two  $(\text{Cu2})\text{O}_4$  squares (green) are connected through  $(\text{B1})\text{O}_4$  tetrahedra in a double path.  $(\text{Cu1})\text{O}_4$  squares are connected with  $(\text{Cu2})\text{O}_6$  distorted octahedra at the apical O atoms. For better visualization, some of the O and B atoms in the unit cell are not shown. Interchain exchange interactions are frustrated and shown by a black dashed line.

temperature- and field-dependent dc-magnetization [ $M(T)$  and  $M(H)$ ] measurements on the oriented  $\text{CuB}_2\text{O}_4$  crystals are performed using a S700X SQUID magnetometer (Cryogenic) and nonmagnetic Cu-Be pressure cells; a piston-cylinder cell (Camcool make, with PTFE capsule having diameter 1.5 mm and length 17 mm) for measurements up to 1.1 GPa and a miniature DAC (EasyLab make, culet diameter 500  $\mu\text{m}$ , Cu-Be gasket, preindented to 80  $\mu\text{m}$  thickness and hole diameter 240  $\mu\text{m}$ ) for measurements up to 6.6 GPa, with daphne oil as pressure medium. The thermomagnetic responses of the empty pressure cells were subtracted to obtain the sample response. Pressures in the DAC were precalibrated at low  $T$  by the ruby luminescence method. For studies on piston-cylinder cells, pressure was determined from the known pressure dependence of superconducting  $T_c$  variation of Sn [40].

### III. RESULTS

#### A. X-ray diffraction

Powder diffraction patterns of  $\text{CuB}_2\text{O}_4$  at various high pressures at 300 K are shown in Fig. 2(a). The patterns remain almost unchanged with increasing pressures indicating overall phase stability of the ambient tetragonal structure (space group  $I\bar{4}2d$ ,  $z = 12$ ) at least up to 25 GPa. Figure 2(b) shows the typical Rietveld fitted diffraction pattern at high pressure. Due to the large set of refinable structure parameters in the fitting, our analysis does not give any pressure-induced systematic of the positional coordinates of the O and B atoms. Fittings using the reported positional coordinates [41] of ambient pressure give reasonable good fits for all pressures supporting the above claim. The  $\text{CuO}_4$  square blocks and the  $\text{BO}_4$  tetrahedron at high pressures thus evolves primarily through lattice parameter change. Pressure variation of the lattice parameters [shown in Fig. 2(c)] indicates anisotropic

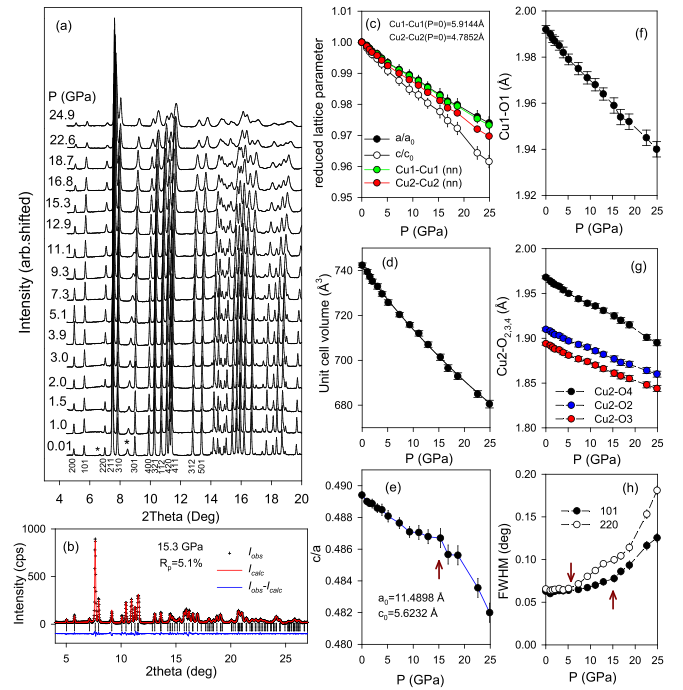


FIG. 2. (a) X-ray diffraction patterns of  $\text{CuB}_2\text{O}_4$  (for wavelength 0.4957  $\text{\AA}$ ) at various high pressures, shown after subtracting the DAC background pattern. Some of the  $(hkl)$  indices are shown at the bottom. Peaks marked with an asterisk correspond to quartz impurity, as contaminated at the time of grinding of the crystal. (b) Rietveld fitted diffraction pattern at 15.3 GPa. Pressure variations of (c) the reduced lattice parameters along with the reduced nearest-neighbor Cu-Cu distances, (d) the unit cell volume, fitted with equation of state, (e) the  $c/a$  ratio, (f) Cu1-O and (g) Cu2-O bond distances, and (h) the FWHM of the (101) and (220) Bragg peaks.

compressibility. Tetragonal  $c$ -axis compressibility is about 30% higher than the  $ab$ -plane compressibility. Pressure variation of the unit cell volume [Fig. 2(d)], when fitted with the third-order Birch equation of state [42], gives the bulk modulus  $220 \pm 5$  GPa (with  $B' = 5.2 \pm 0.3$ ). However, a distinct change in the compression anisotropy can be noticed [see Fig. 2(e)]. The  $c/a$  ratio decreases monotonically up to  $\sim 15$  GPa above which this ratio decreases more rapidly. Whereas, the Cu-O bond distances at both Cu positions ( $4b$  and  $8d$  sites) reduce monotonically with increasing pressure [see Figs. 2(f) and 2(g)]. Also, a closer look at the diffraction patterns shows that even though the individual Bragg peaks remain distinguishable at all pressures, an increased peak broadening is noticed at high pressure [see Fig. 2(h)]. While both (101) and (220) Bragg peaks broaden rapidly above 15 GPa, the (220) peak FWHM starts increasing at  $P \sim 5$  GPa. These observations hint for emergence of structural disorder or subtle structural transition at these pressures, possibly by lowering the tetragonal point group symmetry (as discussed in detail with the results of Raman and IR phonon measurements). A somewhat similar peak broadening is noticed in XRD measurements with different pressure media (MEW and silicone oil), ruling out the effect of nonhydrostatic compression and thus the intrinsic nature of the peak broadening is confirmed.

## B. Phonon studies

The primitive unit cell of  $\text{CuB}_2\text{O}_4$  contains 42 atoms, resulting in 126 normal modes. Due to noncentrosymmetric crystal structure, infrared active polar modes are also Raman active. Group-theoretical analysis predicts the following Brillouin zone-center vibrational modes [43]:  $\Gamma_{\text{Raman}} = 13A_1 + 14B_1 + 17B_2 + 31E(2)$  (106 modes),  $\Gamma_{\text{IR}} = 17B_2 + 31E(2)$  (79 modes),  $\Gamma_{\text{Silent}} = 17A_2$ ;  $\Gamma_{\text{Acoustic}} = B_2 + E(2)$ .

The detailed phonon structure of  $\text{CuB}_2\text{O}_4$  at ambient pressure has been reported by analyzing polarization-dependent Raman scattering and IR spectroscopic measurements and by density functional theory calculations [34,35]. In addition to the successful identification of the complete set of zone-center optical modes by symmetry analysis, IR absorption has revealed a set of multiphonon bands. As high-pressure polarized Raman measurement with liquid pressure medium often causes polarization leakage due to change in crystal orientation and pressure-induced birefringence in diamonds, we have first performed an unpolarized Raman scattering measurement on the (001) flat sample. Figure 3(a) shows the Raman spectra in the spectral range 100–1200  $\text{cm}^{-1}$  at the initial pressure ( $P = 0.6$  GPa). The spectrum comprises of a large number of sharp modes in the low-frequency region below 500  $\text{cm}^{-1}$ . These are identified by comparing the reported results [34,35]. In the backscattering geometry of our high-pressure Raman measurements,  $(A_1 + B_2)$  and  $B_1$  symmetry modes are only expected from the possible  $z(x'x')\bar{z}$  and  $z(x'y')\bar{z}$  scattering configurations, respectively. However, some in-plane  $E$ -symmetry modes are also found in the spectrum resulting from crystal misalignment, causing polarization leakage. Based on the calculation of the bond length variations in various modes, Pisarev *et al.* [34] have succeeded in assignment of these low-frequency modes. The modes below 200  $\text{cm}^{-1}$  are localized vibrations of the Cu atom, whereas modes in the range 200–500  $\text{cm}^{-1}$  are essentially the Cu-O vibrations. There are four characteristic localized modes of the Cu(4b) atom:  $B_1$  at 149  $\text{cm}^{-1}$  and  $B_2$  at 154  $\text{cm}^{-1}$  are oscillations along the  $z$  axis and  $E$  modes at 212 and 222  $\text{cm}^{-1}$  are in-plane oscillations. The modes at 112 and 144  $\text{cm}^{-1}$  correspond to the  $B_2$  and  $E$  vibrations, respectively, of the Cu(8d) atom. The observed Cu(4b)  $E$  modes at 212 and 222  $\text{cm}^{-1}$  are weak in intensity and are overlapped with the  $B_2$  mode of Cu(8d).

In Fig. 3(b) we have followed the pressure evolution of various Cu localized modes marked as M1–M4. While Cu4b-related M3 and M4 modes remain mostly unchanged with increasing pressure up to 22 GPa, the M1 and M2 modes show abrupt changes at high pressures. The M1 mode corresponding to the Cu-8d oscillation along the  $z$  axis gains intensity rapidly above 4 GPa, and starts broadening and splitting above 12 GPa. For the M2 mode corresponding to the in-plane oscillation of the Cu(8d) atom, intensity vanishes above this pressure. These clearly indicate a pressure-induced structural modification with change in Cu(8d) site symmetry. The observed systematic frequency softening at high pressures of the localized modes can be due to the decreased size of the octahedra and square plaquette. In the spectral range of 300–500  $\text{cm}^{-1}$ , three strong  $A_1$  symmetry modes are clearly distinguishable from several weaker modes from other

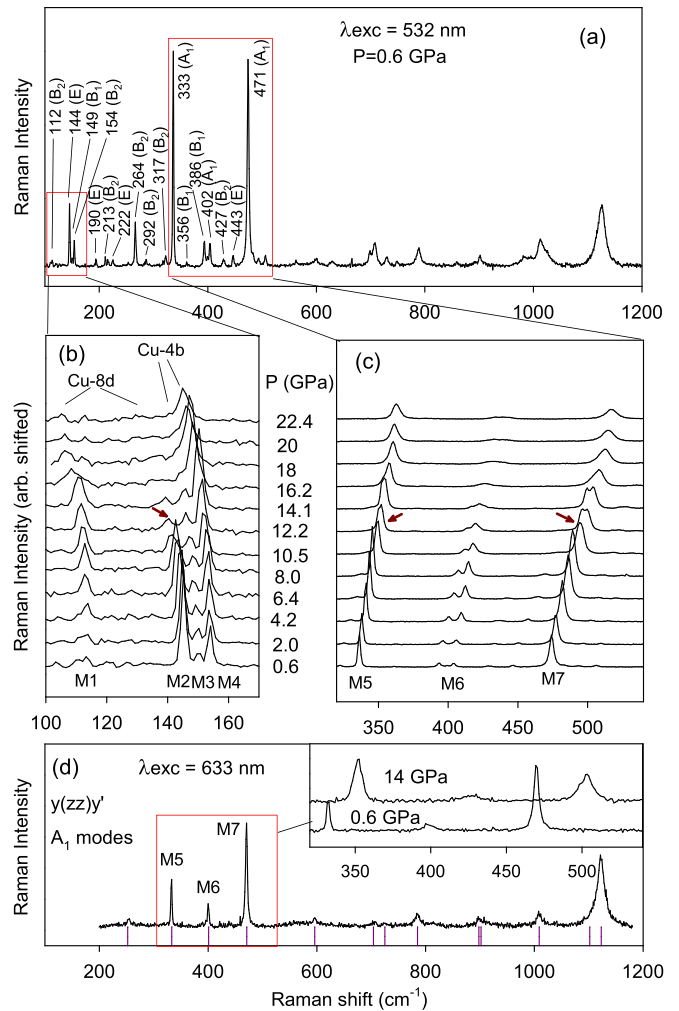


FIG. 3. (a) Unpolarized Raman spectra from the (001) flat surface of the  $\text{CuB}_2\text{O}_4$  crystal at 0.6 GPa at room temperature. Frequencies and mode symmetry are indicated for the low-frequency peaks. Raman spectra at various high pressures in the spectral ranges (b) 100–170  $\text{cm}^{-1}$  and (c) 300–550  $\text{cm}^{-1}$ . (d) Polarized Raman spectra from the oriented crystal in the  $y(zz)y'$  configuration at 0.6 GPa. The vertical lines at the bottom indicate reported  $A_1$  symmetry mode frequencies [34,35]. The inset shows polarized Raman spectra in the range 300–550  $\text{cm}^{-1}$  at 0.6 and 14 GPa.

symmetry. The  $A_1$  modes are marked with M5 (333  $\text{cm}^{-1}$ ), M6 (402  $\text{cm}^{-1}$ ), and M7 (471  $\text{cm}^{-1}$ ). The mode at 386  $\text{cm}^{-1}$  is identified as of  $B_1$  symmetry. In Fig. 3(c) is plotted the pressure variation of the spectra in this frequency range. All these modes show pressure-induced systematic stiffening up to 22.4 GPa. A clear splitting of the M5 and M7 modes is noticed above 12 GPa, supporting the structural transition at this pressure. As the  $A_1$  symmetry modes are relatively strong and do not mix with other symmetry modes, the splitting can be considered to occur within the  $A_1$  modes. To further confirm this, we have performed the polarized Raman measurements at high pressure on the (010)-oriented flat crystal in the  $y(zz)y'$  configuration [see Fig. 3(d)]. All 12  $A_1$  symmetry modes can be identified comparing with the reported data [34,35]. The inset shows the spectra in the range 300–500  $\text{cm}^{-1}$  at 0.6

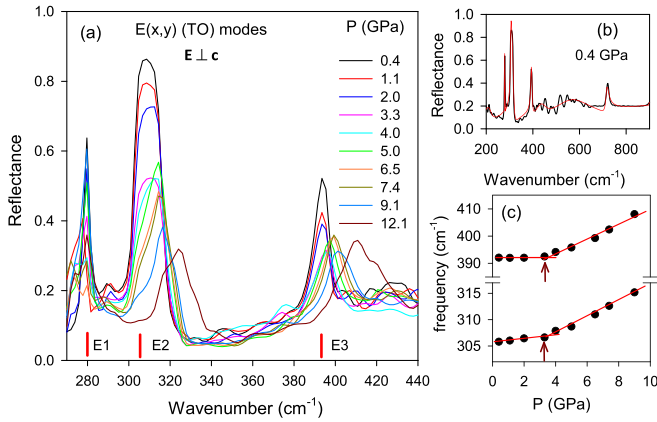


FIG. 4. (a) Room-temperature IR reflectance spectra at the diamond-sample interface  $R_{s-d}$  from the (001) surface of the  $\text{CuB}_2\text{O}_4$  crystal at various pressures. Vertical lines at the bottom indicate polar  $E(x, y)$  modes in the reported IR spectra at ambient pressure [34]. (b) A typical fit with the damped Lorentz oscillator model is shown in red for spectra at 0.4 GPa. (c) Pressure variation of the peak frequencies of the  $E2$  and  $E3$  modes. Straight lines are guides to the eye showing a rapid change in slope across 3 GPa. Arrows indicate the pressure where an anomalous slope change occurs.

and 14 GPa. Significant broadening with the emergence of shoulder peaks at 14 GPa clearly indicates splitting of the  $A_1$  modes confirming the structural transition. Pressure variations of the observed Raman modes are shown in the Supplemental Material [44].

Figure 4(a) shows infrared reflectance spectra from  $\text{CuB}_2\text{O}_4$  single crystal measured at various high pressures using a synchrotron IR source with polarization of the incident light in the plane of the (001) crystal surface. This allowed us to probe the  $E(x, y)$  symmetry TO-polar optical modes. The peak frequency and intensity of various IR modes have been obtained by analyzing the reflectance spectra using the REFFIT program [45]. In Fig. 4(b) is shown the fitted far-IR reflectance spectrum for the lowest pressure (0.4 GPa), where we identify three strong polar phonon modes marked as  $E1$ ,  $E2$ , and  $E3$  at 280, 305, and 392  $\text{cm}^{-1}$ , respectively. These modes correspond to the Cu-O vibrations associated with the  $\text{Cu}(8d)\text{O}_6$  octahedra and the obtained mode parameters agree well with the reported values at ambient pressure [34]. Upon increasing pressure, the  $E2$  and  $E3$  modes show an anomalous change in slope of their pressure variation of the peak frequencies near 3 GPa [see Fig. 4(c)]. Also, beyond this pressure the  $E2$  mode strength decreases rapidly. These results indicate structural modification at  $\sim 3$  GPa. This can also be correlated with the onset of the (220) XRD peak broadening near 5 GPa [Fig. 2(f)] and a rapid intensity gain of the  $\text{Cu}(8d)$  localized vibration of the  $B_2$  symmetry at 112  $\text{cm}^{-1}$  above 4 GPa [Fig. 3(b)]. At this point, the details of this structural modification are not clearly understood, but this is associated with the modification of the  $\text{Cu}(8d)$  site environment. At 12 GPa, a conspicuous change in the reflectance spectra is clearly noticed where both  $E2$  and  $E3$  modes show significant broadening with emergence of shoulder peaks. This splitting of the  $E(x, y)$  modes further supports the structural transition as corroborated by our XRD and Raman measurements at this pressure.

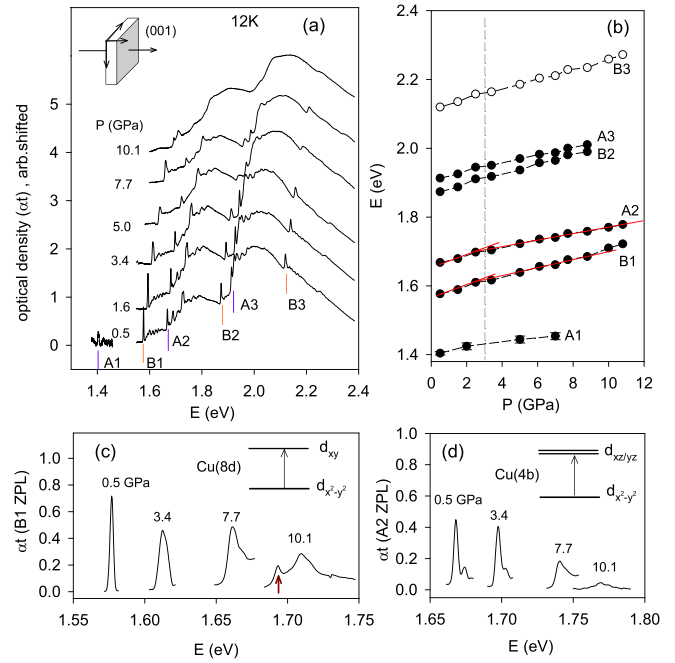


FIG. 5. (a)  $\alpha$ -absorption spectra with light propagation along the tetragonal  $c$  axis of  $\text{CuB}_2\text{O}_4$  at 12 K at some selected high pressures. The scale of optical density ( $\text{OD} = \alpha t$ ,  $\alpha =$  absorption coefficient,  $t =$  crystal thickness) is shown for the spectra at 0.5 GPa. For higher pressures, plots are arbitrarily shifted vertically for easy comparison of their pressure evolution. The zero-phonon transitions (ZPLs) corresponding to Cu  $4b$  and  $8d$  sites are marked as (A1, A2, A3) and (B1, B2, B3), respectively. (b) Pressure variation of the ZPL peak positions. Red lines indicate anomalous change in pressure-slope near 3 GPa, as also marked by the vertical dashed line. While the error bars for the measured A1 ZPL energy position is relatively large, error bar sizes for other ZPLs are within the symbol size. Pressure evolution of the absorption spectra are shown separately for the (c) B1 and (d) A2 peaks along with the respective  $d-d$  transition schemes.

### C. Optical absorption

In order to understand the effect of structural modification on the  $d-d$  excitations we have performed low-temperature optical absorption studies under high pressure. A 20- $\mu\text{m}$ -thick crystal with (001) flat surface was mounted in a DAC with NaCl as pressure medium and light is incident along the crystallographic  $c$  axis to obtain the  $\alpha$ -absorption spectra, where propagation vector  $k \parallel c$  and electric polarization  $E \parallel a$  (b) [30]. The observed  $\alpha$ -absorption spectrum of  $\text{CuB}_2\text{O}_4$  at 12 K comprises six sharp zero-phonon lines (ZPLs) along with other phonon-assisted broad absorption bands. Figure 5(a) shows the measured optical density ( $\text{OD} = \ln(I_0/I)$ , where  $I$  and  $I_0$  are transmitted light intensity with and without sample, respectively) at selected pressures. The zero-phonon absorption peaks correspond to the  $d-d$  excitations for the two nonequivalent Cu sites in  $\text{CuB}_2\text{O}_4$ . The ZPLs of the crystal-field split  $d-d$  transitions for the Cu(4b) site are marked as A1, A2, and A3 and those for the Cu(8d) site are marked as B1, B2, and B3. The absorption spectra and the ZPL peak energies at the lowest pressure (0.5 GPa) agree well with

the reported results of ambient pressure measurement [18,30]. The spectral features remain almost unchanged up to  $\sim 3$  GPa, above which the features of ZPLs as well as other phonon-assisted absorption bands change abruptly. In Figs. 5(c) and 5(d) we show the evolution of the  $B1$  and  $A2$  ZPLs, respectively, with increasing pressures. Here we have plotted the ZPL absorption OD after subtracting the broad background. As the resolution of the observed  $A1$  line is poor in our high-pressure measurement due to low detector response in this range, we are unable to follow the pressure evolution of this ZPL with accuracy. The  $B1$  line corresponds to the intrasite  $d_{x^2-y^2}$  to  $d_{xy}$  electric-dipole transition of the  $\text{Cu}^{2+}$  ion in the  $8d$  site. This zero-phonon transition results in a Gaussian peak with a narrow width (FWHM  $\sim 2$  meV) at the initial pressure without exhibiting any signature of Davydov or exchange-related splitting at this site symmetry, unlike the  $A1$  transition at the  $4b$  site [23,31]. At 3.4 GPa, a significant broadening of the  $B1$  line indicates subtle structural modification affecting the  $\text{Cu}(8d)$  site environment. A symmetry-allowed enhanced  $\text{Cu}(8d)\text{O}_6$  octahedral distortion/local disorder may be attributed to the increased linewidth of this ZPL peak at high pressure. Moreover, somewhat shorter Cu-O bond length causes larger Cu-O orbital overlapping at the  $8d$  site compared to the  $\text{Cu}(4b)$  atoms. As a result, the  $\text{Cu}(4b)$  ZPL  $A2$  remains narrow up to 3.4 GPa whereas the  $B1$  line shows significant broadening at this pressure [see Figs. 5(c) and 5(d)]. The structural modification at this pressure may be correlated with the observed changes in pressure dependence of the polar  $E(x, y)$  IR phonon modes and Raman anomalies near 3 GPa. Site-selective absorption study thus clearly indicates that the  $\text{Cu}(8d)$  site environment modification is responsible for this anomalous change. The broad peak feature of the  $B1$  line remains unchanged up to 7.7 GPa before a drastic change occurs near 10 GPa. The emergence of a new absorption peak at a lower energy [shown by the up arrow in Fig. 5(c)] indicates an abrupt structural modification at this pressure, associated with the structural transition at 12 GPa as discussed before. The  $A2$  line corresponds to the  $d_{x^2-y^2}$  to  $d_{xz,yz}$  transitions for the  $\text{Cu}^{2+}$  ion at the  $4b$  site. While the initial study of this line reported degenerate  $d_{xz,yz}$  levels [18,30], high-resolution measurement later confirmed the SOC driven splitting of the  $d_{xz,yz}$  levels [23]. In Fig. 5(d) we show the pressure evolution of the  $A2$  line that comprises two peaks of unequal intensity. This absorption band remains unchanged up to  $\sim 5$  GPa, above which its intensity decreases gradually with no sign of broadening and finally vanishes at 10.1 GPa. Systematic intensity reduction and subsequently vanishing of this absorption line at further high pressure is attributed to the induced disorder and/or structural inhomogeneity, causing forbidden electric-dipole transition. A detailed understanding on the pressure-induced dramatic suppression of the ZPL intensity in the high-pressure structure warrant further theoretical and experimental investigations. In Fig. 5(b) we show the pressure dependence of the ZPL peak energies. With increasing pressure, the peak energies increase monotonically, except showing subtle anomalous slope change near 3 GPa. The pressure-induced systematic blueshifting of overall absorption spectra including the ZPLs is consistent with the systematic

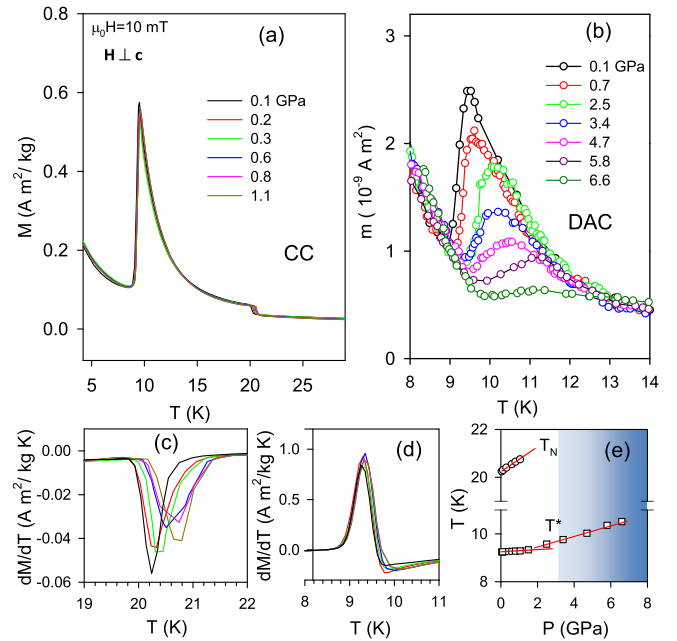


FIG. 6. (a) Plots of dc magnetization of  $\text{CuB}_2\text{O}_4$  crystal as a function of temperature,  $M(T)$ , with 10 mT magnetic field applied perpendicular to the tetragonal  $c$  axis for pressures up to 1.1 GPa using a piston-cylinder cell (CC) and (b) the magnetic moment,  $m(T)$ , measured up to 6.6 GPa using a miniature DAC. Derivative  $dM/dT$  plots are shown (c) near AFM Néel temperature  $T_N$  and (d) at the commensurate-incommensurate transition temperature  $T^*$ . (e) Pressure variation of the  $T_N$  and  $T^*$ . Red lines are linear fits in different  $T$  ranges. The shaded region indicates the magnetic phase with large  $T^*$  slope, possibly due to pronounced  $\text{Cu}(8d)_6$  distortion.

decrease in the Cu-O bond lengths, causing increased Cu- $d$  and O- $p$  orbital overlap for both Cu sites at high pressures.

#### D. Magnetic measurements

To understand the effect of hydrostatic pressure on the magnetic ordering and transitions, we have performed dc-magnetization measurements on  $\text{CuB}_2\text{O}_4$  with a 10 mT magnetic field applied perpendicular to the tetragonal  $c$  axis. Measurements have been performed on oriented single crystal (size  $\sim 1 \times 1 \times 0.6$  mm, weight  $\sim 2.5$  mg) at pressures up to 1.1 GPa using a piston-cylinder cell [see Fig. 6(a)]. For measurements at higher pressures (up to 6.6 GPa), a miniature DAC has been employed and a small oriented single crystal (size  $\sim 200 \times 180 \times 40$   $\mu\text{m}$ ) are used [see Fig. 6(b)]. The low-pressure data clearly show two magnetic transitions. High- $T$  paramagnetic phase orders into a canted AFM phase below Néel temperature  $T_N \sim 20$  K and subsequently undergoes a transition into the incommensurate-helical (IC-HC) ordered phase below  $T^* \sim 9.2$  K, agreeing with our magnetization measurement on the bare sample [44]. The magnetic ordering temperatures have been evaluated from the peaks of the derivative plots of the magnetization curve, as shown in Figs. 6(c) and 6(d). Upon increasing pressure,  $T_N$  increases at the rate 0.5 K/GPa, whereas  $T^*$  remains mostly pressure independent. Due to the large paramagnetic background moment of DAC, the signature of AFM transition of  $\text{CuB}_2\text{O}_4$  near 20 K

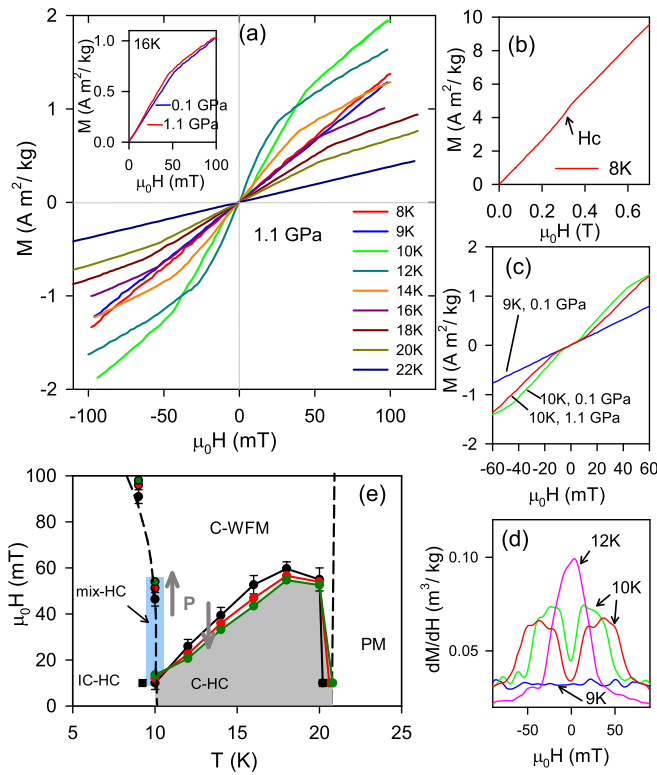


FIG. 7. (a) Magnetization  $M(H)$  plots of  $\text{CuB}_2\text{O}_4$  crystal at 1.1 GPa at various low temperatures with magnetic field applied perpendicular to the tetragonal  $c$  axis. The inset shows the  $M(H)$  plots at two pressures at 16 K. (b)  $M(H)$  plot at 8 K shows IC-C magnetic transition near the 0.3 T field. (c) Expanded view of the  $M(H)$  plots at 9 and 10 K at two pressures. (d) Derivative  $dM/dH$  plots at 9, 10, and 12 K. 10-K data are shown for two pressures (0.1 and 1.1 GPa). (e) Evolution of the magnetic ( $H$ - $T$ ) phase diagram for  $\text{CuB}_2\text{O}_4$  with increasing pressures. The symbols for 0.1, 0.5, and 1.1 GPa are shown in black, red, and green, respectively. The light-blue shaded region is the mixed phase region of the IC-helical and C-helical spin structures.

is not well resolved in DAC-based measurement and hence we are unable to follow its pressure evolution beyond 1.1 GPa. With increasing pressure the asymmetric peak feature in the magnetic moment plot  $m(T)$  at the C-IC phase transition near 9 K gradually decreases and this becomes barely visible above 6 GPa [Fig. 6(b)]. The  $P$ - $T$  phase diagram with the magnetic field 10 mT applied perpendicular to the tetragonal  $c$  axis is shown in Fig. 6(e).

For better understanding of the effect of pressure on the stability of the magnetic phases in the  $H$ - $T$  phase diagram, we have performed high-pressure magnetization  $M(H)$  measurements with field applied perpendicular to the tetragonal  $c$  axis. Figure 7(a) shows the magnetization  $M(H)$  plots at various temperatures at 1.1 GPa. For  $T > T_N \sim 20$  K, a linear  $M(H)$  curve with slope representing paramagnetic susceptibility is observed up to high applied field. In the temperature range  $10 \text{ K} \leq T \leq 20 \text{ K}$ , a quasilinear  $M(H)$  behavior is noticed up to a critical field above which a saturation magnetization is developed due to the emergence of weak ferromagnetic ordering in the commensurate phase. The low-field magnetic ordering is known to be of long-period helical spin order [2, 11]. With

increasing pressure the critical field decreases and the saturation magnetization increases [see inset in Fig. 7(a)]. Due to systematic suppression of the critical field under high pressure, the phase boundary is pushed downward [see Fig. 7(e)]. The application of hydrostatic pressure thus favors the WFM ordering. It is noteworthy that the novel magneto-optical and magnetoelectric phenomena occur in the WFM phase. Thus  $\text{CuB}_2\text{O}_4$  may exhibit these properties at a lower field and with more pronounced feature by application of external pressure.

For  $T < T^*$ , the incommensurate (IC) helical ordered state remains stable with linear  $M(H)$  curve up to a high field, but a clear change in the  $M(H)$  slope is detected at higher field where the system evolves into the commensurate (C) weakly ferromagnetic phase [see Fig. 7(b)]. Although this transition is preceded by a metamagnetic transition to another incommensurate phase (IC') with a different helical pitch and with the formation of soliton lattice at its border [15], no anomaly has been observed in the magnetization curve at a lower field [10]. A careful observation of the magnetization data near the C-IC transition shows an opposite trend of the pressure effect on the IC phase. The IC-C transition field increases with pressure, showing a higher stability of the incommensurate state under pressure. In Figs. 7(c) and 7(d) we plot the  $M(H)$  curves at 9 and 10 K and their pressure dependencies, respectively. A comparison of the  $M(H)$  slope at 10 K with that of 9 K clearly indicates that incommensurate-helical (IC-HC) order is present at 10 K below 10 mT. Whereas, a C-WFM ordering (with emergence of saturation magnetization) occurs above 45 mT. The  $M(H)$  curve in the field range 10–45 mT is very different than that in the commensurate ordered (C-HC) phase at higher temperature. Based on the  $dM/dH$  plots [Fig. 7(d)], we conclude that the region of phase diagram at 10 K in the field range 10–45 mT represents a mixed phase region of IC-helical and C-helical spin structures. This has been indicated by the light-blue shaded area in Fig. 7(e).

#### IV. DISCUSSION

Let us first discuss the results of the observed structural transition in  $\text{CuB}_2\text{O}_4$ . The intrinsic XRD peak broadening above 12 GPa can be associated with a structural transition to a space group having an unchanged tetragonal lattice parameter, where the O and B positions are allowed to move more randomly due to a reduced site symmetry. A group-subgroup analysis thus suggests the most probable structural transition ( $I\bar{4}2d$  to  $I\bar{4}$ ). In the new space group, Cu(8d) atoms and its connecting O atoms take Wyckoff position 8g, allowing them to move along the  $x$ ,  $y$ , and  $z$  directions, unlike the 8d site of the initial space group that allows only  $x$ -coordinate movement. This can lead to atomic disordering and loss of interplanar coherence which results in enhanced peak broadening as well as a rapid reduction in  $c/a$  ratio. In the new structure with space group  $I\bar{4}$ , group-theoretical analysis predicts the following zone-center vibrational modes:  $\Gamma_{\text{Raman}} = 30A + 31B + 31(^1E + ^2E)$  (123 modes),  $\Gamma_{\text{IR}} = 31B + 31(^1E + ^2E)$  (93 modes),  $\Gamma_{\text{Acoustic}} = B + ^1E + ^2E$ .

The  $17A_2$  silent modes of the low-pressure tetragonal phase (space group  $I\bar{4}2d$ ) become Raman active in the high-pressure structure with new space group  $I\bar{4}$ . This is clearly evident from the observed splitting of the strong  $A_1$  Raman modes

above 12 GPa. Also the  $E(x, y)$  modes become nondegenerate ( ${}^1E + {}^2E$ ) in this structure, as clearly evident by the distinct emergence of the shoulder peaks of the IR  $E(x, y)$  modes. The optical absorption spectra above 10 GPa shows that near the Cu(8d)-related B1 ZPL a new strong absorption peak is emerged at 20 meV below the initial peak. The splitting of the ZPL at high pressure could be due to distinct crystal-field splitting of the emerged Cu(8g) site environment with two distinct apical O(8g) atoms in their octahedron. Due to the large unit cell of CuB<sub>2</sub>O<sub>4</sub> with a large number of refinable O and B positions, we were unable to determine the subtle change in O positions by the Rietveld analysis to confirm the above structural modification. These observations thus demand a high-resolution structural investigation at high pressure. The structural modification in CuB<sub>2</sub>O<sub>4</sub> near 3 GPa is more subtle and can be ascribed to enhanced distortion of the Cu(8d)O<sub>6</sub> octahedra.

Now we discuss the effect of pressure on various magnetic phases of CuB<sub>2</sub>O<sub>4</sub>. Pressure-induced structural modification causes change in magnetic interactions. Due to significant anisotropic compression, DM interaction, exchange anisotropy, and spin frustration get modified. The observed enhanced saturation magnetization in the weakly ferromagnetic phase under pressure can be understood in terms of enhanced DM interaction. A moderate increase of the Néel temperature  $T_N$  with somewhat unchanged paramagnetic susceptibility at high pressure (up to 1.1 GPa) can be attributed to a systematic increase of the nearest-neighbor exchange interaction ( $J_1$ ) in the 3D Heisenberg AFM strong Cu(4b) sublattice ( $T_N \propto J_1$ ). In the commensurate canted AFM phase, increasing of pressure reduces systematically the turnup field of the weak ferromagnetic order [see Fig. 7(e)]. It has been shown by Petrova and Pankrats [10] that as the measurement field exceeds the turnup field at a temperature, dc susceptibility saturates causing drastic suppression of its magnitude near the C-IC transition. In the present study, a rapid suppression of magnetic moment  $m(T)$  with 10 mT field near the C-IC transition at high pressure [Fig. 6(b)] can be interpreted in terms of significant decrease in the turnup field for the WFM order. Vanishing of the magnetic moment peak feature at 10 K above 6 GPa indicates that the maximum critical field decreases to

as low as 10 mT. Pressure-induced suppression of the critical field may also be associated with an increase of the saturation magnetization due to increased DM interaction. Due to higher  $c$ -axis compressibility [see Fig. 2(c)], next-nearest-neighbor exchange interaction ( $J_2$ ) along the crystallographic  $c$  axis (see Fig. 1) plays a crucial role in modifying the magnetic structure at higher pressure [7], mostly affecting the zigzag-chain type weak spin subsystem  $B$  of Cu(8d) sites resulting in enhancement of spin frustration. This explains systematic pressure-driven enhancement of the critical field for helical to WFM phase transition below  $T^*$  and also systematic increase of  $T^*$  at constant field, as shown in Fig. 7(e) ( $T^* \propto J_2$ ) [7]. A detailed quantitative analysis of the pressure evolution of the spin sublattices is beyond the scope of this work. A dc-magnetization study with magnetic field applied along the tetragonal  $c$  axis will be crucial to understand the effect of pressure on the spin frustration of the Cu(8d) sublattice.

In summary, pressure-induced structural evolution of CuB<sub>2</sub>O<sub>4</sub> by powder x-ray diffraction, Raman scattering, and infrared phonon measurements have been reported up to  $\sim 25$  GPa. The system undergoes a structural transition at  $\sim 12$  GPa, preceded by an anomalous structural modification near 3 GPa. Optical absorption measurement at low temperature gives clear evidence of Cu(8d) site symmetry change at the structural transition. High-pressure magnetization measurements have been performed on single crystals with magnetic field applied perpendicular to the tetragonal  $c$  axis. While hydrostatic pressure up to 1.1 GPa favors commensurate WFM phase above  $T^* \sim 9.2$  K, pressure helps to stabilize the incommensurate helical spin structure below  $T^*$ .

## ACKNOWLEDGMENTS

High-pressure XRD investigations have been performed at Elettra synchrotron under Proposal IDs 20125159 and 20195291. IR measurements at Elettra synchrotron were performed under Proposal ID 20110182. Financial support from DST, Government of India is gratefully acknowledged. P.M. acknowledges DST-INSPIRE program for financial support.

- 
- [1] G. Petrakovskii, D. Velikanov, A. Vorotinov, A. Balaev, K. Sablina, A. Amato, B. Roessli, J. Schefer, and U. Staub, *J. Magn. Magn. Mater.* **205**, 105 (1999).
  - [2] G. A. Petrakovskii, A. I. Pankrats, M. A. Popov, A. D. Balaev, D. A. Velikanov, A. M. Vorotynov, K. A. Sablina, B. Roessli, J. Schefer, A. Amato *et al.*, *Low Temp. Phys.* **28**, 606 (2002).
  - [3] M. Boehm, B. Roessli, J. Schefer, A. S. Wills, B. Ouladdiaf, E. Lelievre-Berna, U. Staub, and G. A. Petrakovskii, *Phys. Rev. B* **68**, 024405 (2003).
  - [4] B. Roessli, J. Schefer, G. A. Petrakovskii, B. Ouladdiaf, M. Boehm, U. Staub, A. Vorotinov, and L. Bezmaternikh, *Phys. Rev. Lett.* **86**, 1885 (2001).
  - [5] S. Martynov, G. Petrakovskii, and B. Roessli, *J. Magn. Magn. Mater.* **269**, 106 (2004).
  - [6] S. Martynov, G. Petrakovskii, M. Boehm, B. Roessli, and J. Kuldac, *J. Magn. Magn. Mater.* **299**, 75 (2006).
  - [7] T. Fujita, Y. Fujimoto, S. Mitsudo, T. Idehara, T. Saito, Y. Kousaka, S. i. Yano, J. Akimitsu, J.-i. Kishine, K. Inoue *et al.*, *J. Phys. Soc. Jpn.* **77**, 053702 (2008).
  - [8] S. N. Martynov and A. D. Balaev, *J. Exp. Theor. Phys. Lett.* **85**, 649 (2007).
  - [9] S. N. Martynov, *J. Exp. Theor. Phys. Lett.* **90**, 55 (2009).
  - [10] A. E. Petrova and A. I. Pankrats, *J. Exp. Theor. Phys.* **126**, 506 (2018).
  - [11] A. I. Pankrats, G. A. Petrakovskii, M. A. Popov, K. A. Sablina, L. A. Prozorova, S. S. Sosin, G. Szymczak, R. Szymczak, and M. Baran, *J. Exp. Theor. Phys. Lett.* **78**, 569 (2003).
  - [12] A. Pankrats, G. Petrakovskii, V. Tugarinov, K. Sablina, L. Bezmaternykh, R. Szymczak, M. Baran, B. Kundys, and A. Nabialek, *J. Magn. Magn. Mater.* **300**, e388 (2006).
  - [13] A. Fukaya, I. Watanabe, K. Yamada, and K. Nagamine, *J. Phys. Soc. Jpn.* **75**, 113705 (2006).

- [14] Y. Yasuda, H. Nakamura, Y. Fujii, H. Kikuchi, M. Chiba, Y. Yamamoto, H. Hori, G. Petrákovskii, M. Popov, and L. Bezmaternikh, *J. Phys.: Condens. Matter* **19**, 145277 (2007).
- [15] Y. Kousaka, S. Yano, M. Nishi, K. Hirota, and J. Akimitsu, *J. Phys. Chem. Solids* **68**, 2170 (2007).
- [16] T. Kawamata, N. Sugawara, S. M. Haidar, T. Adach, T. Noji, K. Kudo, N. Kobayashi, Y. Fujii, H. Kikuchi, M. Chiba *et al.*, *J. Phys. Soc. Jpn.* **88**, 114708 (2019).
- [17] Y. Kousaka, S.-i Yano, J.-i Kishine, Y. Yoshida, K. Inoue, K. Kikuchi, and J. Akimitsu, *J. Phys. Soc. Jpn.* **76**, 123709 (2007).
- [18] R. V. Pisarev, I. Sanger, G. A. Petrákovskii, and M. Fiebig, *Phys. Rev. Lett.* **93**, 037204 (2004).
- [19] M. Saito, K. Ishikawa, S. Konno, K. Taniguchi, and T. Arima, *Nat. Mater.* **8**, 634 (2009).
- [20] N. D. Khanh, N. Abe, K. Kubo, M. Akaki, M. Tokunaga, T. Sasaki, and T. Arima, *Phys. Rev. B* **87**, 184416 (2013).
- [21] M. Saito, K. Taniguchi, and T. Arima, *J. Phys. Soc. Jpn.* **77**, 013705 (2008).
- [22] T. Arima, *J. Phys.: Condens. Matter* **20**, 434211 (2008).
- [23] K. N. Boldyrev, R. V. Pisarev, L. N. Bezmaternykh, and M. N. Popova, *Phys. Rev. Lett.* **114**, 247210 (2015).
- [24] S. Toyoda, N. Abe, and T. Arima, *Phys. Rev. B* **93**, 201109(R) (2016).
- [25] S. Toyoda, N. Abe, and T. Arima, *Phys. Rev. Lett.* **123**, 077401 (2019).
- [26] J. Mund, D. R. Yakovlev, A. N. Poddubny, R. M. Dubrovin, M. Bayer, and R. V. Pisarev, *Phys. Rev. B* **103**, L180410 (2021).
- [27] A. D. Molchanova and K. N. Boldyrev, *Opt. Spectrosc.* **127**, 33 (2019).
- [28] M. Saito, K. Ishikawa, K. Taniguchi, and T. Arima, *Phys. Rev. Lett.* **101**, 117402 (2008).
- [29] S. W. Lovesey and U. Staub, *J. Phys.: Condens. Matter* **21**, 142201 (2009).
- [30] R. V. Pisarev, A. M. Kalashnikova, O. Schops, and L. N. Bezmaternykh, *Phys. Rev. B* **84**, 075160 (2011).
- [31] N. E. Kopteva, D. Kudlacik, D. R. Yakovlev, M. V. Eremin, A. R. Nurmukhametov, M. Bayer, and R. V. Pisarev, *Phys. Rev. B* **105**, 024421 (2022).
- [32] S. Toyoda, N. Abe, S. Kimura, Y. H. Matsuda, T. Nomura, A. Ikeda, S. Takeyama, and T. Arima, *Phys. Rev. Lett.* **115**, 267207 (2015).
- [33] J. N. Hancock, G. Chabot-Couture, Y. Li, G. A. Petrákovskii, K. Ishii, I. Jarrige, J. Mizuki, T. P. Devereaux, and M. Greven, *Phys. Rev. B* **80**, 092509 (2009).
- [34] R. V. Pisarev, K. N. Boldyrev, M. N. Popova, A. N. Smirnov, V. Y. Davydov, L. N. Bezmaternykh, M. B. Smirnov, and V. Y. Kazimirov, *Phys. Rev. B* **88**, 024301 (2013).
- [35] V. G. Ivanov, M. V. Abrashev, N. D. Todorov, V. Tomov, R. P. Nikolova, A. P. Litvinchuk, and M. N. Iliev, *Phys. Rev. B* **88**, 094301 (2013).
- [36] R. D. Mero, C.-H. Lai, C. H. Du, and H. L. Liu, *J. Phys. Chem. C* **125**, 4322 (2021).
- [37] M. Martínez-Ripoll, S. Martínez-Carrera, and S. GarciaBlanco, *Acta Crystallogr., Sect. B: Struct. Sci., Cryst. Eng. Mater.* **27**, 677 (1971).
- [38] A. Hammersley, *Computer Program FIT2D* (ESRF, Grenoble, 1998).
- [39] A. C. Larson and R. B. von Dreele, *Los Alamos Report No. LAUR 86-748*, Los Alamos National Laboratory, New Mexico, 1986.
- [40] A. Eiling and J. S. Schilling, *J. Phys. F: Met. Phys.* **11**, 623 (1981).
- [41] G. K. Abdullaev and K. S. Mamedov, *J. Struct. Chem.* **22**, 637 (1981).
- [42] F. Birch, *J. Geophys. Res.* **91**, 4949 (1986).
- [43] M. I. Aroyo, J. M. Perez-Mato, D. Orobengoa, E. Tasci, G. de la Flor, and A. Kirov, *Bulg. Chem. Commun.* **43**, 183 (2011).
- [44] See Supplemental Material at <http://link.aps.org/supplemental/10.1103/PhysRevB.107.094411> for dc magnetization, specific heat measurements on bare sample, and pressure variations of Raman modes.
- [45] A. B. Kuzmenko, *Rev. Sci. Instrum.* **76**, 083108 (2005).